



Prediction of diffusivity and conversion of *n*-decane and CO in coated Pt/ γ -Al₂O₃ catalyst depending on porous layer morphology



Michal Dudák^a, Vladimír Novák^{a,b}, Petr Kočí^{a,c,*}, Miloš Marek^{a,c},
Patricia Blanco-García^b, Glenn Jones^b

^a Institute of Chemical Technology, Prague, Department of Chemical Engineering, Technická 5, Prague 166 28, Czech Republic

^b Johnson Matthey Technology Centre, Blounts Court Road, Sonning Common, Reading RG4 9NH, United Kingdom

^c New Technologies Research Centre, University of West Bohemia, Univerzitní 8, Pilsen 306 14, Czech Republic

ARTICLE INFO

Article history:

Received 30 September 2013

Received in revised form

10 December 2013

Accepted 11 December 2013

Available online 20 December 2013

Keywords:

Diffusion

Exhaust gas aftertreatment

Diesel oxidation catalyst

CO and *n*-decane oxidation

Multi-scale modeling

ABSTRACT

The conversion in monolith reactors for automotive exhaust gas aftertreatment can be limited by diffusion in the catalytic layer. This is particularly important for monolith reactors with multiple coated layers. In this paper, we present detailed modeling methodology for prediction of effective diffusivity based on the actual structure of a porous coating (particle and pore size distributions). We demonstrate the approach on diffusion and oxidation of *n*-decane and CO in Pt/ γ -Al₂O₃ layers typically used in diesel oxidation catalysts. To validate the model predictions experimentally, several layers were coated with uniform thickness on flat metal foils, and their macroporous structure was controlled by alumina particle size distribution, pore templates and compaction techniques. A multi-scale modelling approach was then applied to predict effective diffusivity and impact of the internal diffusion limitations on the achieved conversions. Diffusion of CO and *n*-decane was simulated on a micro-scale together with oxidation reactions in a 3D digitally reconstructed porous layer structure. The results were combined with a macroscopic 1D plug-flow model to calculate the reactor outlet conversions. Good agreement was achieved between the predicted and the measured conversions both for *n*-decane and CO oxidation. The predicted effective diffusion coefficients D^{eff} through the tested Pt/ γ -Al₂O₃ layers were 1.4, 3.6 and $6.4 \times 10^{-6} \text{ m}^2 \text{ s}^{-1}$ for CO at $T = 298 \text{ K}$ in compact, standard and macropore-templated sample, respectively. The corresponding diffusivities for *n*-decane were 0.53, 1.2 and $2.0 \times 10^{-6} \text{ m}^2 \text{ s}^{-1}$, respectively. The model quantified relative contributions of volume and Knudsen diffusion regimes to overall transport as well as temperature dependence of D^{eff} .

© 2013 Elsevier B.V. All rights reserved.

1. Introduction

The catalytic layer deposited on the walls of monolith channels in automotive exhaust gas converters consists of meso- or microporous particles (e.g., γ -Al₂O₃, CeO₂, zeolites) with internal pore sizes below 50 nm and high specific surface area that allows dispersion of active metal sites. Macropores are present between the support particles as shown in schematic Fig. 1 and their typical size ranges from 0.1 μm up to several microns. The particle size distribution (PSD) of the supporting material influences the resulting macroporosity [1]. The conversion of reactants can be limited by transport both in flowing gas phase [2] and inside porous catalytic coating [1,3,4]. The internal transport is particularly relevant to monoliths with multiple coated layers, where the active sites

in the bottom layer are accessible only by the diffusion through the top layer [5–7]. Volume diffusion in macropores is essential for efficient transport of reactants through the layer, because Knudsen diffusion regime in small pores is significantly slower (Fig. 1). Understanding and quantification of the internal diffusion effects are thus pre-requisites for design of optimum catalytic coating in monolith reactors.

A common approach to prediction of the internal diffusion effects used in the automotive industry relies on 1D+1D (or 1D+effectiveness factor) simulations of a monolith channel, where the coated catalytic layer is considered to have uniform thickness and transport properties are represented by an effective diffusion coefficient [8]. This effective diffusivity is typically calculated from random pore model correlation [9] that combines contributions of small meso/micro-pores (intrinsic nanostructure of the used material, slow Knudsen diffusion) and larger macropores (microstructure influenced by the coating procedure, faster volume diffusion). More complex computational strategies for non-uniform distribution of washcoat are available as well [10,11].

* Corresponding author. Tel.: +420 22044 3293; fax: +420 22044 4320.

E-mail addresses: petr.koci@vscht.cz (P. Kočí), gjones@matthey.com (G. Jones).

URL: <http://www.vscht.cz/monolith> (P. Kočí).

Nomenclature

| | |
|-------------------|---|
| a | density of external geometric surface area (GSA), $\text{m}^2 \text{m}^{-3}$ of reactor |
| c | gas concentration, mol m^{-3} |
| c_p | heat capacity, $\text{J kg}^{-1} \text{K}^{-1}$ |
| C_{Pt} | concentration of active catalytic sites (Pt), mol m^{-3} |
| d | diameter, m |
| D | diffusion coefficient, $\text{m}^2 \text{s}^{-1}$ |
| E_a | activation energy of reaction step, $\text{J mol}^{-1} \text{K}^{-1}$ |
| E_{inh} | inhibition exponential factor, K |
| k | kinetic constant of reaction step, dimension depends on reaction order |
| k_0 | pre-exponential factor of kinetic constant, dimension depends on reaction order |
| k_c | mass transfer coefficient, m s^{-1} |
| k_h | heat transfer coefficient, $\text{J m}^{-2} \text{K}^{-1} \text{s}^{-1}$ |
| K_{inh} | kinetic constant of inhibition, dimension depends on reaction order |
| $K_{\text{inh}0}$ | pre-exponential factor of inhibition, dimension depends on reaction order |
| L | length of the reactor, m |
| M | molar weight, kg mol^{-1} |
| p | pressure, Pa |
| r | transverse coordinate in the washcoat layer, m |
| R | reaction rate, $\text{mol m}^{-3} \text{s}^{-1}$ |
| R^g | universal gas constant, $8.314 \text{ J mol}^{-1} \text{K}^{-1}$ |
| t | time, s |
| T | temperature, K |
| V | volume, m^3 |
| \mathbf{x} | vector of spatial coordinates, $\mathbf{x} = (x, y, z)$ |
| x | spatial coordinate, m |
| y | spatial coordinate, m |
| Y | component mole fraction, 1 |
| z | spatial coordinate (longitudinal in the case of monolith), m |

Greek letters

| | |
|---------------|--|
| α | effective heat exchange coefficient of the used lab reactor, 1 |
| τ | tortuosity factor, 1 |
| ε | porosity, 1 |
| δ | thickness, m |
| ΔH_r | reaction enthalpy, J mol^{-1} |
| φ^w | vol. fraction of washcoat in solid phase (incl. wall), 1 |
| λ | heat conductivity, $\text{J m}^{-1} \text{s}^{-1} \text{K}^{-1}$ |
| ν | stoichiometric coefficient, 1 |
| ρ | density, kg m^{-3} |
| σ | volume diffusion constant, $\text{m}^3 \text{mol}^{-1}$ |

Subscripts and superscripts

| | |
|-------|------------------------|
| bnd | boundary |
| e | external (surrounding) |
| eff | effective |
| g | gas |
| i | index of gas component |
| j | index of reaction |
| Kn | Knudsen diffusion |
| m | monolith |
| M | macro-pores |
| μ | meso-pores |
| p | particle |
| Pt | platinum particles |

| | |
|-----|----------------------------------|
| s | solid phase, in full-scale model |
| s | substrate + coating |
| t | total |
| vol | volume diffusion |
| w | porous coating, washcoat |

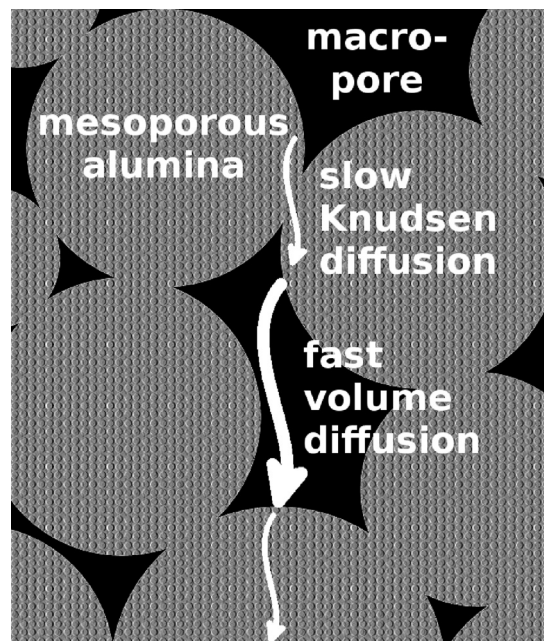


Fig. 1. Schematic drawing of diffusion in porous coated layer, involving both macro- and meso-pores.

However, all monolith channel models critically depend on the use of accurate effective diffusion coefficients, otherwise they give misleading predictions of the diffusion limitations. So far, only a few reports have been published on the measured diffusivity in catalytic washcoats that suggested approximate values with relatively large uncertainties [12–16].¹ In all reported cases, the transport coefficients were fitted to measured data, but the experiments were arranged in several different ways. The aim was either to observe steady-state diffusion flux through monolith wall from one channel to another [14], or to apply transient inverse gas chromatography technique [15], or to quantify the diffusional limitations from light-off experiments under specific conditions combined with 1D modeling approach [16]. However, these methods are generally not able to link the fitted effective diffusivity to actual structure of the investigated porous layer. Furthermore, the fitted results do not reveal relative contributions of volume and Knudsen diffusion to the overall effective diffusivity. As both mechanisms depend on temperature and weight/size of gas molecule to a different extent, the extrapolation of fitted diffusivities to other components or temperatures remains uncertain.

In contrast, our modeling methodology focuses on accurate prediction of the effective diffusivity based on actual structure of the coated porous layer, and therefore can serve as coating design and optimization tool. This approach is based on 3D digital

¹ When reviewing different diffusivity values reported in literature, it should be strictly distinguished between overall transport through the macroporous layer, and local diffusion in small meso/micro-pores with an order-of-magnitude lower diffusivity. This difference is sometimes ignored and incompatible diffusivity values are then compared together [16].

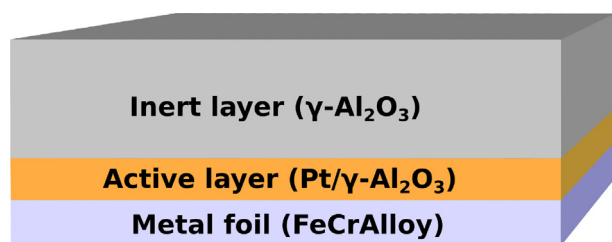


Fig. 2. Configuration of the prepared samples.

reconstruction of the porous coating utilizing information from cross-section SEM images and/or particle and pore-size distributions, and subsequent simulation of diffusion and reaction in the reconstructed medium [1,17,18]. In our recent paper [1], the predicted effective diffusivities were first confronted with the experimental data for CO oxidation under diffusion-limited regime in a lab-scale reactor with standard coated Pt/ γ -Al₂O₃ layers. The results indicated that this detailed approach could provide more accurate predictions of diffusivity than the conventional random pore model correlation [9], at least in the range of the studied layer structures with macroporosities 26–36%.

In this paper we significantly extend the range of examined layer morphologies by those prepared with pore templates or compaction techniques, resulting in structures with a much wider range of macroporosity (17–54%). In addition to CO, we also investigate *n*-decane as a representative of heavier, slowly diffusing hydrocarbons (typical for diesel engine exhausts) in order to prove the predictive power of the model for various gas components. Through the comparison of simulations with experiments, we validate the capability of the proposed detailed model to predict the effective diffusivity accurately in a wide range of porous structure morphologies. Full temperature dependence of the effective diffusivity is obtained from simulations, and relative contributions of volume and Knudsen diffusion to overall transport are discussed. The presented approach clearly illustrates how the coated layer structure translates into effective diffusivity values, and subsequently, how the effective diffusivity influences achieved conversions in the reactor.

2. Experiments

2.1. Preparation and characterization of catalytic layers

Several Pt/ γ -Al₂O₃ coated metal foils were prepared in order to build-up set of catalyst samples suitable for experimental validation of model predictions. First, a thin active Pt/ γ -Al₂O₃ layer was coated. This active layer (the same for all samples) was then overlaid with an additional inert γ -Al₂O₃ layer of a defined morphology that was different for the individual samples. This additional layer did not contain Pt and served as a diffusion barrier for the transport of reactants to the catalytic sites, Fig. 2. This design of samples enabled us to clearly observe the effect of internal diffusion limitations on *n*-decane and CO oxidation, particularly on the residual outlet concentration of the reactants after the light-off.

The layers were coated on laser cut FeCrAlloy foils (thickness 110 μ m), activated before the coating process at 950 °C for 2 h to obtain rough metal surface that aided adhesion by means of physical keying. Coatings were made of commercially sourced and subsequently milled γ -Al₂O₃ micro-particles of the type Puralox (Sasol). Pure alumina was utilized either as a support for dispersed platinum catalyst or as a transport limiting layer. In the former case, solution of standard Pt precursor (Johnson Matthey) was impregnated into the γ -Al₂O₃ particles filling whole volume of pores (incipient wetness method [19,20]), subsequently dried at 130 °C

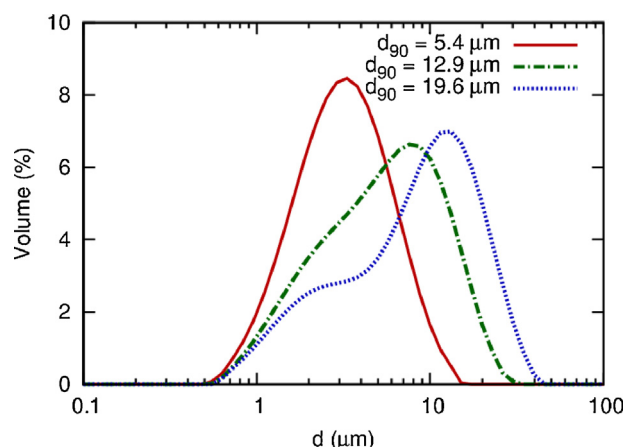


Fig. 3. Particle size distributions of all milled Puralox alumina slurries. The times of milling are given in Table 1.

Table 1

Milling times of all prepared alumina slurries and size of alumina particles after milling at constant speed 3500 rpm.

| | Pt/ γ -Al ₂ O ₃ | γ -Al ₂ O ₃ | |
|-----------------------|--|--|------|
| $d_{p,90}$ (μ m) | 5.4 | 12.9 | 19.6 |
| Time (mm:ss) | 17:00 | 4:30 | 2:55 |

Table 2

Layers configuration of the tested and modeled samples. Sample ID describes the layer type, A stands for active and I for inert layer, following number means layer thickness in microns. Possible modifications are explained in the table. Symbols used: δ = layer thickness, ε_M = macroporosity, \bar{d}_M = mean macropore diameter, $d_{p,90}$ = γ -Al₂O₃ particle size, p = pressure applied to layer compaction (psi), PS = polystyrene particles as macropore templates (volume percent).

| Sample ID | δ (μ m) | ε_M (1) | \bar{d}_M (nm) | $d_{p,90}$ (μ m) | Modification |
|-----------|---------------------|---------------------|------------------|-----------------------|----------------|
| A18 | 18 | 0.18 | 238 | 5.4 | – |
| I125_PS10 | 125 | 0.54 | 571 ^a | 12.9 | 10% (wt.) PS |
| I130 | 130 | 0.35 | 957 | 19.6 | – |
| I95_p100 | 95 | 0.17 | 190 | 12.9 | p = 100 kpsi |

Common properties of γ -Al₂O₃ (Puralox, Sasol) in all layers: skeletal density $\rho = 3.18$ g cm⁻³ (He pycnometry), internal mesoporosity $\varepsilon_\mu^s = 0.54$ (Hg porosimetry), mean mesopore diameter $\bar{d}_\mu = 10$ nm (nitrogen sorption, desorption branch, BJH model), tortuosity of mesopores $\tau_\mu = 1.7$ (typical value for γ -Al₂O₃ [18]).

^a Excluding the large macropores formed by templates.

for 4 h and calcined at 500 °C for 2 h. The final quantity of platinum was 2% by weight.

Both Pt-impregnated and inert aluminas were prepared in the form of a water-based slurry containing 37% of alumina by weight and with pH modified to 4.5 to decrease the viscosity. The slurries were milled separately to reduce their particle size using a bead mill (Mini Motormill 250, Eiger Torrance). Different particle size distributions were obtained, Fig. 3. The particle size distributions were analysed by laser diffraction using MasterSizer 2000 (Malvern Instruments).

Viscosity of the milled slurries was adjusted by pH before coating to obtain uniform crack-free layers. Wire-wounds bars (Longfield Coating & Engineering Products) were used to gain a controlled thickness of the coated layer on the metal foils. Each coated layer was then dried at 50 °C for half an hour and calcined for 2 h at 500 °C.

By this procedure, the same thin active layer (Pt/ γ -Al₂O₃) with particle size $d_{p,90} = 5.4$ μ m was coated on all foils. The overlaid inert layer was different for the individual samples, with macroporosity varied in a wide range (54–17%) from high (by pore templating), through medium (by standard coating) to low (by compaction), cf. Table 2 and Fig. 4. For the pore templating, 10 wt.% of

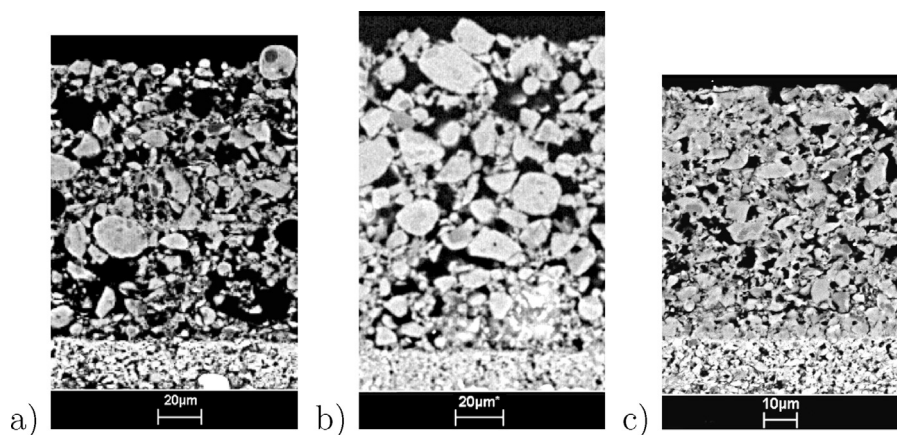


Fig. 4. Cross-section SEM images of prepared catalytic layers: (a) A18+I125.PS10 with templated PS particles, (b) A18+I130 standard layer, (c) A18+I95.p100 compacted sample.

monodisperse polystyrene particles (PS) with diameter $d_{PS} = 15.7 \mu\text{m}$ were suspended in the slurry before coating via a solution of dispersing agent DisperByk-180 (Byk) and ultrasonication (45 kHz, ≈ 5 min). Polystyrene particles were chosen as material available in a variety of sizes, with monomodal particle size distribution, and readily removable by calcination. The amount of PS particles was chosen to increase macroporosity noticeably while preserving mechanical stability of the layer. For the standard inert layer, macroporosity was controlled only by size distribution of alumina particles in the slurry. In the case of compacted samples, the inert layer was coated and dried in standard way, and then pressed at 100 kpsi (Mackey Bowley) in direction perpendicular to the foil surface and finally calcined in standard way.

Morphology of prepared samples was analysed by scanning electron microscope (Leica S440i). The layer thickness and macroporosity were evaluated from the obtained SEM images. Narrow mesopore size distribution with mean mesopore size \bar{d}_μ of 10 nm was evaluated by nitrogen sorption data using BJH method on desorption branch (Autosorb-1, Quantachrome Instruments). The internal mesoporosity $\varepsilon_\mu^s = 54\%$ (related to the volume of alumina particles) of both milled and unmilled alumina was determined from mercury porosimetry data (AutoPore IV, Micromeritics Instrument). Both intraparticle parameters (\bar{d}_μ and ε_μ^s) remained unaffected by sample preparation procedure.

The mean macropore size for individual coated layers was also evaluated from mercury porosimetry data, cf. Fig. 5a. The large macropores formed inside the layer by thermal decomposition of PS particles cannot be detected by this technique—mercury can be intruded into them only after passing smaller macropores that serve as bottlenecks, so that their volume is attributed to smaller pores. To reveal the large macropores formed from templates, maximum sphere inscription (MSI) method [18] was applied to the reconstructed medium for comparison (Fig. 5b). The accuracy of the MSI method in the range of small macropores is limited by the used spatial discretization step.

Skeletal density of the alumina ρ_s was 3.175 g cm^{-3} (AccuPyc II 1340 Helium Pycnometer, Micromeritics Instrument). The amount of active platinum sites in the active layer (Pt/ $\gamma\text{-Al}_2\text{O}_3$) was determined by CO chemisorption (AutoChem II 2920, Micromeritics Instrument) to be $30.9 \mu\text{mol g}^{-1} \text{ cat}$ (30% metal dispersion). This value was converted to the volume basis using density of alumina particles including mesopores $\rho_p = \rho_s(1 - \varepsilon_\mu^s)$, so that the concentration of active Pt sites was calculated $C_{Pt}^\mu = 44.8 \text{ mol m}^{-3}$ of washcoat excluding macropores.

The structural properties of individual samples are summarized in Table 2. The prepared samples are denoted according to layer type, its thickness and inert layer modification. For example A18+I125.PS10 means sample with Active layer 18 μm thick

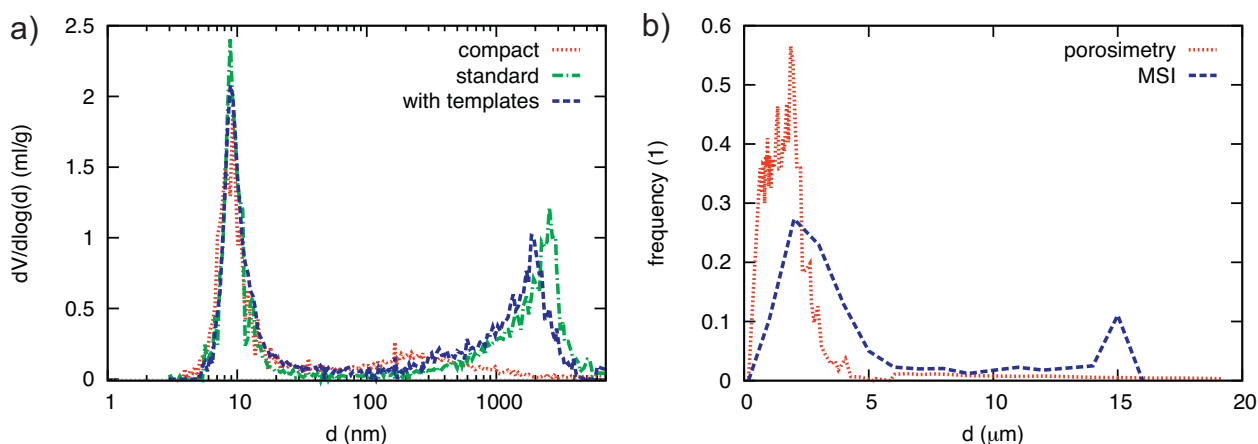


Fig. 5. Pore size distributions: (a) for standard, compact and macropore-templated layers evaluated from mercury porosimetry, (b) comparison of porosimetry and maximum sphere inscription (MSI) method of the macropore-templated sample.

Table 3
Lab reactor configuration and inlet gas parameters.

| Parameter | Value | |
|--|---------------------------------------|---------------------------------------|
| | <i>n</i> -Decane | CO |
| Coated foil length | | 30 mm |
| Coated foil width | | 25 mm |
| No. of identical foils in the stack | | 4 |
| Total height of the stack | | 4.5 mm |
| Total volume of the stack | | 3.38 cm ³ |
| Metal foil thickness | | 110 μm |
| Washcoat thickness (different samples) | | 18–148 μm |
| Flow rate (STP) | 0.5 dm ³ min ^{−1} | 1.0 dm ³ min ^{−1} |
| Inlet Y_i | 300 ppm (mol.) | 0.5% (mol.) |
| Inlet Y_{O_2} | 2.0% (mol.) | 1.5% (mol.) |

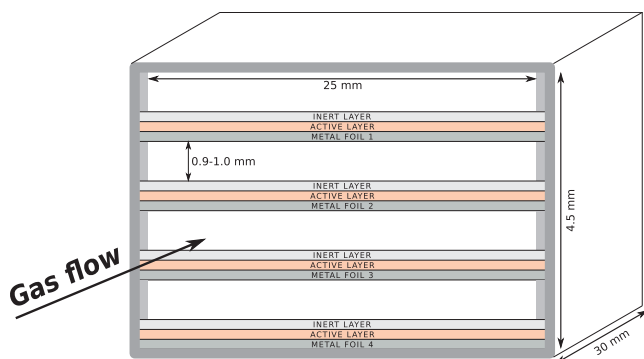


Fig. 6. Schematic arrangement of samples in the reactor, cross-section in plane perpendicular to flow direction.

(A18) covered by Inert layer 125 μm thick (I125) with 10 wt.% of polystyrene templates (PS10).

2.2. CO and *n*-decane oxidation measurements

To obtain experimental data for model validation, CO and decane light-off curves were measured in a nearly isothermal mini-reactor commonly used for testing of standard monolith samples [1,21]. The apparatus consists of cylinders with pressurised gases, mass flow controllers (Bronkhorst EL-Flow), decane liquid flow controller (L01-Liqui-MicroFlow, 0.02–0.4 g/h) and controlled evaporation-mixing unit (Bronkhorst CEM), flat-bed steel reactor with heating and analytical instruments (FTIR MKS 2030HS, ABB MAGNOS 16).

A holder with four identical coated foils was placed in the reactor (Fig. 6), with two thermocouples positioned before and after the holder. The gap between the foils in the holder was ca. 1 mm, which roughly corresponds to the characteristic diameter of a standard monolith channel. Other relevant parameters of the reactor are summarized in Table 3. When determining the operating flow rate, the initial examined flow rate 4 dm³ min^{−1} was repeatedly halved down to the point where the influence of external mass transfer on the outlet conversion with the A18 sample safely diminished, i.e., full conversion was achieved above the light-off temperature with the thin single active layer as shown in Fig. 9. The external diffusion effects were accounted for in the model of entire reactor (described in detail later), and the corresponding simulation did not reveal any limitation of the outlet conversion by external mass transfer (Fig. 9). This flow rate was then fixed and used as standard flow rate in all experiments. Note that lower mass transfer coefficients of decane enforced the use of lower flow-rate (Table 3). The corresponding transverse Peclet number (ratio of the characteristic time of component diffusion between two plates to the characteristic time of gas convection along the channel) was ca. 0.10 for CO and 0.18 for decane.

Prior to the oxidation light-off measurements, the samples were stabilized by 1 h oxidation/reduction cycling at 500 °C (1 min 1.5% O₂/1 min 1% H₂ for 50 min and final 10 min 1% H₂ only) and then cooled down in nitrogen. Then, slow temperature ramps (3 K/min) were performed in the range 100–350 °C to obtain a complete decane and CO light-off curves. The pipelines were heated up to 230 °C to prevent decane adsorption/condensation. The inlet mixture was prepared from individual synthetic gases (for decane: 300 ppm C₁₀H₂₂, 2.0% O₂, N₂ balance; for CO: 0.5% CO, 1.5% O₂, N₂ balance) using online mass flow controllers. The decane and CO outlet concentrations were measured by FT-IR (MKS 2030HS). Each light-off experiment was repeated at least twice to check that the catalyst activity was stable. Prior to each subsequent temperature ramp, the catalyst was reduced 10 min by 1% hydrogen at 450 °C and then cooled down in N₂. The measured temperature increase between the inlet and outlet did not exceed 10 °C.

3. Mathematical modeling

To predict the effective diffusivity in the porous layer and its impact on the conversions, we employ and further extend the pore-scale model of transport and reactions in a 3D digitally reconstructed porous layer that has been developed in our group [17,22–24]. Diffusion in macropores between alumina particles is treated as a combination of volume and Knudsen diffusion, while the transport in small pores inside the support particles is approximated by pseudo-homogeneous Knudsen diffusion. The results of this pore-scale model were recently validated for CO diffusion and oxidation in standard coated Pt/γ-Al₂O₃ layers [1]. In this paper we extend the model application to a wider range of porous structures (to validate the predictions also for low- and high-macroporosity layers) and also to *n*-decane diffusion and oxidation (to validate the predictions for heavier hydrocarbon molecules typically present in diesel exhaust).

We further compare the detailed 3D pore-scale model results with the conventional approach that employs random-pore correlation [9] for estimation of effective diffusivity and 1D diffusion in a pseudo-homogeneous slab representing the layer as a whole. The random pore correlation is the most suitable for this application, because it correctly considers bimodal nature of pores in the coated layer (large macropores and small meso/micro-pores) and its predictive power is based only on the actual porous structure of the layer (porosities and pore sizes measured by porosimetry analysis), excluding any adjustable parameters like tortuosity that are freely used to adjust the predictions in other correlations.

Both considered models of porous catalytic coating, i.e., (i) detailed 3D pore-scale model, and (ii) conventional random-pore correlation together with a 1D slab model, are then coupled with a standard 1D plug-flow model of the entire reactor that enables prediction of outlet concentrations and conversions. We denote these

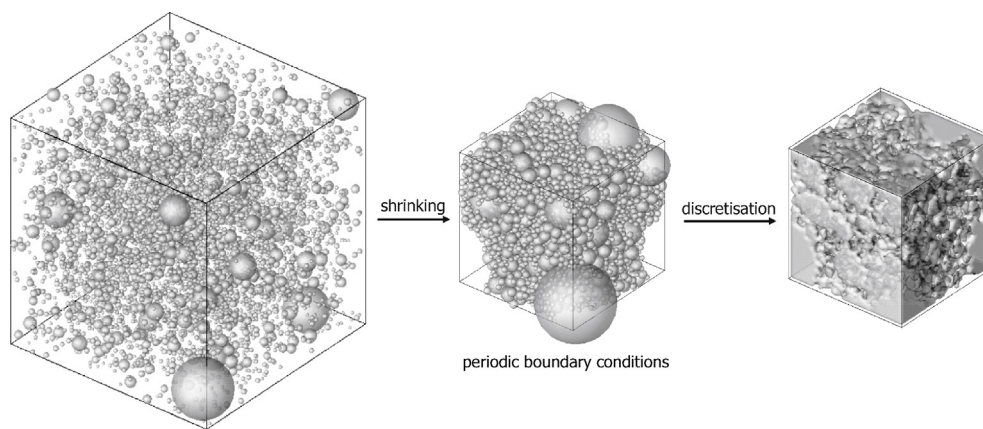


Fig. 7. Steps in the 3D digital reconstruction of a porous layer by the discrete element method and final transformation into the discrete phase function.

two resulting model combinations as (i) detailed multi-scale model, and (ii) standard 1D + 1D model, respectively.

3.1. 3D pore-scale model of catalytic layer

First, the macroporous structure of a catalytic layer was digitally reconstructed using the discrete element method with the given particle size distribution (PSD) of the milled alumina. Spherical γ - Al_2O_3 particles were generated randomly in a defined virtual box according to the PSD, and particle packing was simulated by shrinking the box size with a simplified force model until the predefined macroporosity was reached. The obtained porous media were then transformed to a discrete phase function in the form of

3D matrix containing the information about the phase in each volume discretization element – voxel. A constant voxel size of 250 nm was used in the discretised media. The reconstruction steps are illustrated in Fig. 7. The multi-layer coatings consisting of layers with different PSD or macroporosity were reconstructed individually layer by layer and then stacked together to a final structure, cf. Fig. 8.

The spatially 3D diffusion and reaction model utilizes the digitally reconstructed porous layer with typical dimension on the order of hundreds of microns. Isothermal conditions are considered in this scale, because the temperature gradients are typically in the order of 0.1 K over the simulated system [26]. The 3D steady-state diffusion and reaction model of catalytic layer is described by the

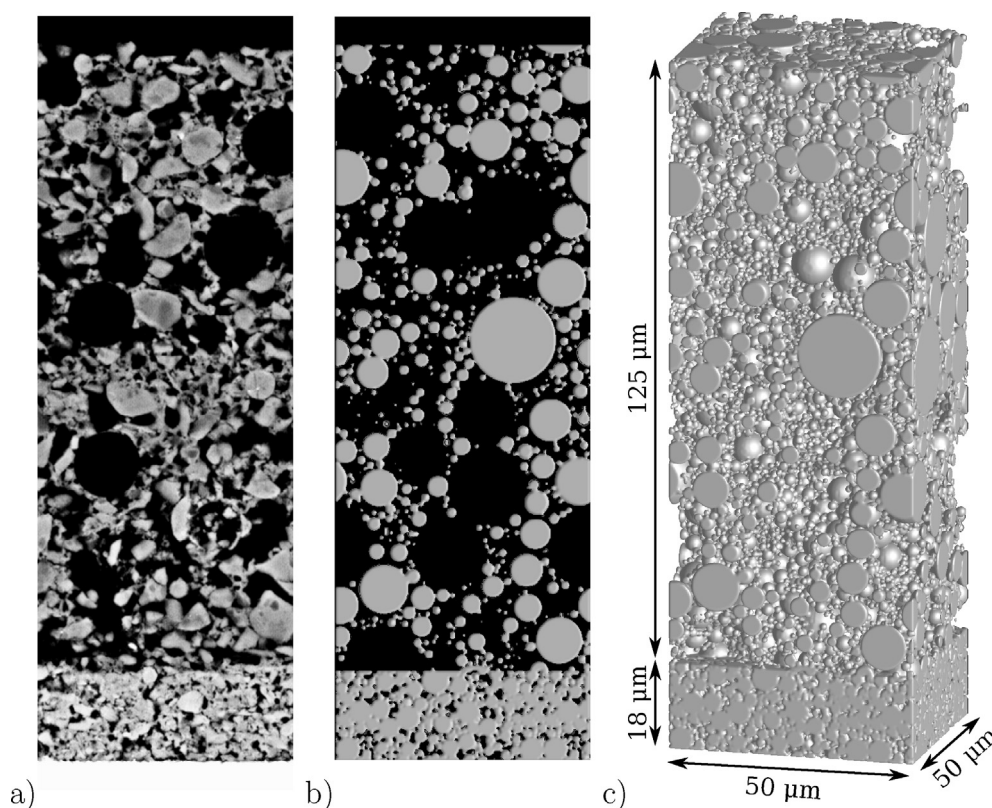


Fig. 8. Structure of the coating A18+I125.PS10 with templated PS particles: (a) cross-section SEM image, (b) cross-section of the reconstructed coating, (c) 3D digital reconstruction.

following mass balances of the gas components $i = 1 \dots I$, involving reactions $j = 1 \dots J$ [1]:

$$\nabla \cdot (D_i \nabla Y_i) + \sum_{j=1}^J \nu_{i,j} \cdot R_j = 0 \quad (1)$$

After equidistant spatial discretization with the step equal to voxel size of the reconstructed medium (250 nm in this work), the set of partial differential equations (1) is solved iteratively by an aggregation-based algebraic multigrid method [1,27].

The “solid phase” (γ -Al₂O₃ particles) includes implicitly internal mesopores so that the balances for the gas components are considered there as well [1]. The reactions take place only inside the mesoporous γ -Al₂O₃ particles in the active layer where the Pt is impregnated. The local concentration of active Pt sites is represented by a 3D function $C_{Pt}(\mathbf{x})$. Uniform distribution of Pt inside the supporting γ -Al₂O₃ particles was assumed in the model.

The following boundary conditions are applied: constant component concentrations on the boundary with the source of the reactants, and zero flux on the other boundaries [22]. The source of the reactants is only at the external surface of the washcoat layer (boundary with the bulk gas in the channel, in this paper z_1 , oriented to the page top).

$$Y_i|_{z=z_1} = Y_i^{\text{bnd}} \quad (2)$$

$$\left. \frac{\partial Y_i}{\partial x} \right|_{x=x_0, x_1} = 0, \quad \left. \frac{\partial Y_i}{\partial y} \right|_{y=y_0, y_1} = 0, \quad \left. \frac{\partial Y_i}{\partial z} \right|_{z=z_0} = 0 \quad (3)$$

Here, Y_i^{bnd} is boundary molar fraction of the component i .

The local (spatially dependent) diffusion coefficients $D_i(\mathbf{x})$ are calculated from Eq. (4) accounting for the combined contribution of volume (6) and Knudsen diffusivity (7).

$$\frac{1}{D_i(\mathbf{x})} = \frac{1}{\psi(\mathbf{x})} \left(\frac{1}{D_i^{\text{Kn}}(\mathbf{x})} + \frac{1}{D_i^{\text{vol}}} \right) \quad (4)$$

The factor $\psi(\mathbf{x})$ is equal to 1 in the defined macropore space. Inside the supporting particles, the $\psi(\mathbf{x})$ accounts for the effects of internal mesoporosity ε_μ^s and tortuosity of mesopores τ_μ , because mesopore space is not discretised in the applied model scale:

$$\psi(\mathbf{x}) = \begin{cases} 1, & \text{if } \mathbf{x} \in \text{macropore} \\ \frac{\varepsilon_\mu^s}{\tau_\mu}, & \text{if } \mathbf{x} \in \text{mesoporous solid phase} \end{cases} \quad (5)$$

The following correlation for volume diffusivity of the component i in the reference gas “ref” is used [28]:

$$D_i^{\text{vol}} = \frac{1.449 \times 10^{-2} T^{1.75}/p}{\sqrt{2/(10^{-3}/M_i + 10^{-3}/M_{\text{ref}})(\sigma_i^{1/3} + \sigma_{\text{ref}}^{1/3})^2}} \quad (6)$$

Here, σ_i is the diffusion volume of the component i (16.3, 18.0 and 209.8 m³ mol⁻¹ for N₂, CO and decane, respectively) [28]. Nitrogen was considered as a reference component (carrier gas).

Knudsen diffusion coefficient is calculated as follows:

$$D_i^{\text{Kn}}(\mathbf{x}) = \frac{\bar{d}(\mathbf{x})}{3} \sqrt{\frac{8R^s T}{M_i \pi}} \quad (7)$$

Mean macropore and mesopore diameters of individual layers were evaluated from porosimetry (cf. Table 2) and applied as local mean pore diameters $\bar{d}(\mathbf{x})$:

$$\bar{d}(\mathbf{x}) = \begin{cases} \bar{d}_m, & \text{if } \mathbf{x} \in \text{macropore} \\ \bar{d}_\mu, & \text{if } \mathbf{x} \in \text{mesoporous solid phase} \end{cases} \quad (8)$$

3.1.1. Effective diffusion simulations

The desired value of overall effective diffusivity through the reconstructed porous medium (D_i^{eff}) is calculated from the mass fluxes obtained by the simulation of the system with an imposed concentration gradient [1,18] and no reactions, i.e., $\sum_{j=1}^J \nu_{i,j} \cdot R_j = 0$ in Eq. (1). In this case, two different boundary concentrations of the diffusing component i are set at z_0 and z_1 , thus overriding the standard boundary condition at $z=z_0$ given in Eq. (3):

$$Y_i|_{z=z_0} = Y_i^{\text{bnd}, z_0} \quad (9)$$

$$Y_i|_{z=z_1} = Y_i^{\text{bnd}, z_1} \quad (10)$$

The difference between Y_i^{bnd, z_1} and Y_i^{bnd, z_0} acts as a driving force for diffusion in the z -direction. From the converged concentration field, the overall effective diffusivity D_i^{eff} of gas component i is calculated:

$$D_i^{\text{eff}} = -\frac{J_i}{A_z} \frac{L_z}{c(Y_i^{\text{bnd}, z_1} - Y_i^{\text{bnd}, z_0})} \quad (11)$$

Here $L_z = (z_1 - z_0)$ is the thickness of the reconstructed medium in the direction z and J_i is the overall molar flux through the medium, obtained by integrating the fluxes across the cross-section area A_z perpendicular to the z -direction [18]. At steady state there is no net accumulation of mass in the medium, so that:

$$J_i = \int_A -D_i \frac{\partial c_i}{\partial z} dx dy \quad (12)$$

Here D_i is local diffusivity value (i.e., $D_i(\mathbf{x})$), governed by fundamental equations (4)–(7).

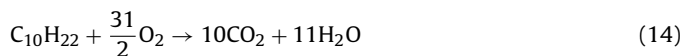
It is also possible to calculate separately the tortuosity factor τ_M of the reconstructed macropore space. In this case only diffusion in macropores is simulated. The resulting calculated tortuosity of macropores is then:

$$\tau_M = \frac{\varepsilon_M D_i}{D_i^{\text{eff}}} \quad (13)$$

It should be noted that the effective diffusivity and tortuosity values are obtained directly from the simulations depending only on the known morphology of the porous structure, without the use of any adjustable parameters. Steady state diffusion simulation at a chosen temperature in detailed 3D pore-scale model that enables prediction of the effective diffusion coefficient takes ca. 10 min on one CPU core of a current common desktop computer. The only specific demand on hardware is somewhat larger RAM (ca. 8–32 GB of memory needed for allocation of 3D matrices with concentration profiles, depending on the size and discretization of the studied system).

3.1.2. Combined reaction and diffusion simulations

In the combined reaction and diffusion simulations, the reaction kinetics for n -decane and CO oxidation in Pt/ γ -Al₂O₃ was considered with the following global reactions:



The reaction rate of both reactant oxidation was described by the pseudo-stationary kinetics of Voltz type (16) [29]. This type of kinetics enabled to describe also the global rate of decane oxidation with sufficient accuracy. Complete oxidation of decane was

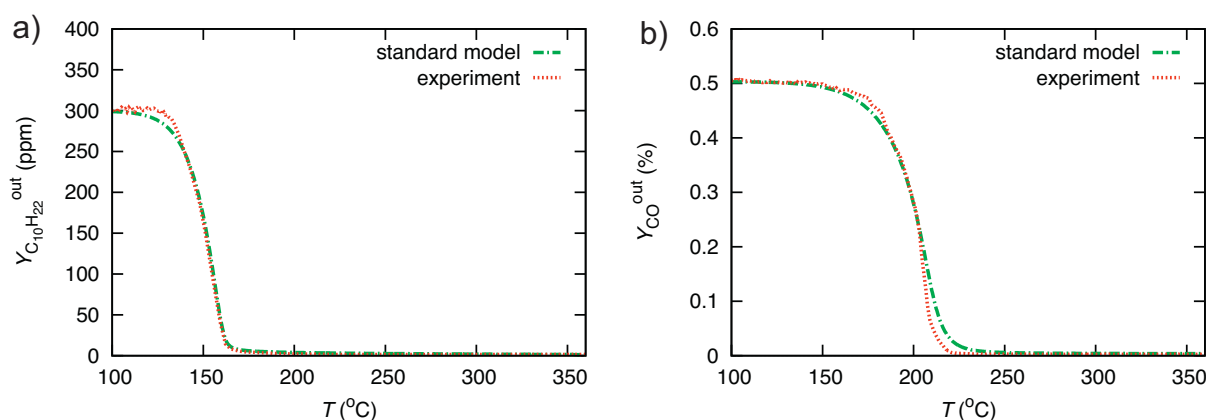


Fig. 9. Light-off curves for (a) decane, and (b) CO oxidation in single active layer A18.

Table 4

The used values of reaction kinetics parameters.

| Parameter | C ₁₀ H ₂₂ oxidation | CO oxidation | Units |
|--------------|---|----------------------|----------------------|
| $k_{0,j}$ | 3.4×10^{17} | 7.4×10^{17} | K s ⁻¹ |
| $E_{a,j}$ | 101×10^3 | 90×10^3 | J mol ⁻¹ |
| $K_{inh0,j}$ | 1.0 | 80.0 | 1 |
| $E_{inh,j}$ | 4.8×10^3 | 1.0×10^3 | K |
| $H_{r,j}$ | -6345 | -283 | kJ mol ⁻¹ |
| C_{Pt}^μ | 44.8 | 44.8 | mol m ⁻³ |

Concentration of catalytic Pt sites (C_{Pt}^μ) is related to net volume of mesoporous γ -Al₂O₃, excluding macropores.

achieved in experiments in agreement with Eq. (14), without any by-products (checked for components measurable by the FTIR).

$$R_j(\mathbf{x}) = \begin{cases} 0, & \text{if } \mathbf{x} \in \text{macropore} \\ C_{Pt}^\mu \frac{k_j Y_i Y_{O_2}}{(1 + K_{inh,j} Y_i)^2 T}, & \text{if } \mathbf{x} \in \text{mesoporous solid phase, for decane oxidation } j=1 \text{ and } i = \text{C}_{10}\text{H}_{22}, \text{ for CO oxidation } j=2 \text{ and } i = \text{CO}. \end{cases} \quad (16)$$

Here, k_j and $K_{inh,j}$ are the rate and the inhibition coefficients, respectively, that are exponentially dependent on temperature:

$$k_j = k_{0,j} \exp\left(\frac{-E_{a,j}}{R^* T}\right) \quad (17)$$

$$K_{inh,j} = K_{inh0,j} \exp\left(\frac{+E_{inh,j}}{T}\right) \quad (18)$$

The kinetic parameters for the oxidation reactions were obtained by fitting of the standard model (cf. Section 3.2) to the light-off curves measured for the single thin active layer A18 (cf. Table 2) without significant external and internal mass transfer limitations as shown in Fig. 9. The activation energies were fixed at the typical values for CO and hydrocarbons oxidation on Pt/ γ -Al₂O₃ in global kinetic models [8]. The remaining parameters were optimised using simplex minimisation method for the sum of squares of differences between simulation results and experimental data [30]. For CO oxidation, the same parameter values as in our previous study were obtained except the slightly modified pre-exponential factor (7.4×10^{17} here vs. 5.0×10^{17} in [1]). The values of kinetic parameters (Table 4) were then fixed and employed in all other simulations.

The goal of this procedure was to obtain a relevant estimate of kinetic parameters for the active layer that could be then used as a basis for validation simulations of the diffusion model in the samples with multiple coated layers. The diffusion model validation is based mainly on the conversions obtained in the fully diffusion-controlled regime (well above the light-off temperature).

The results in this region are determined by transport limitation in the top inert layer and they are quite insensitive to exact values of kinetic parameters in the bottom active layer. Hence any potential inaccuracy in kinetic parameters or rate laws does not influence the results obtained at higher temperatures, which makes the validation procedure very robust.

The concentration of active Pt sites was evaluated from the Pt loading and dispersion (measured by CO chemisorption), including the recalculation from support-mass based to support-volume based concentration of Pt sites. The skeletal density of γ -Al₂O₃ particles $\rho_{\gamma\text{-Al}_2\text{O}_3} = 3.18 \text{ g cm}^{-3}$ and internal mesoporosity $\varepsilon_\mu^s = 0.54$ were considered in these calculations (cf. Table 2).

An example of the reaction rate profile calculated for one of the studied layer configurations is shown in Fig. 10. With increasing temperature, the reaction rate in the active layer becomes

progressively limited by the transport of reactants through the overlaid inert layer and in the end a fully diffusion-limited regime is established.

The spatially averaged reaction rate $R_j^{\text{avg},t}$ is then evaluated for the entire washcoat structure at different temperatures and boundary concentrations:

$$R_j^{\text{avg},t} = \frac{1}{V^t} \int_{V^t} R_j dV, \quad (19)$$

Here, V^t is total volume of the coated layer (including macropores).

3.2. Full-scale model of catalytic reactor

Interpretation of the effect that the catalyst macroporous structure has on its end-use properties is enabled by coupling the model of catalytic layer and the full-scale model of the whole catalytic reactor. A 1D plug-flow model commonly used for exhaust gas aftertreatment simulations in the automotive industry was employed for component mass balances in the flowing gas, and enthalpy balances of the flowing gas and solid phase [8].

Two alternative approaches to the coupling of internal diffusion effects in the coated layers with plug-flow model balances were applied and compared. The first approach relies in the utilization of a spatially averaged effective reaction rate that is pre-calculated by detailed 3D micro-scale simulations discussed above, thereby including all internal diffusion effects (this multi-scale combination is further called “detailed model”). The second, conventional approach solves simplified 1D diffusion model in the porous layer

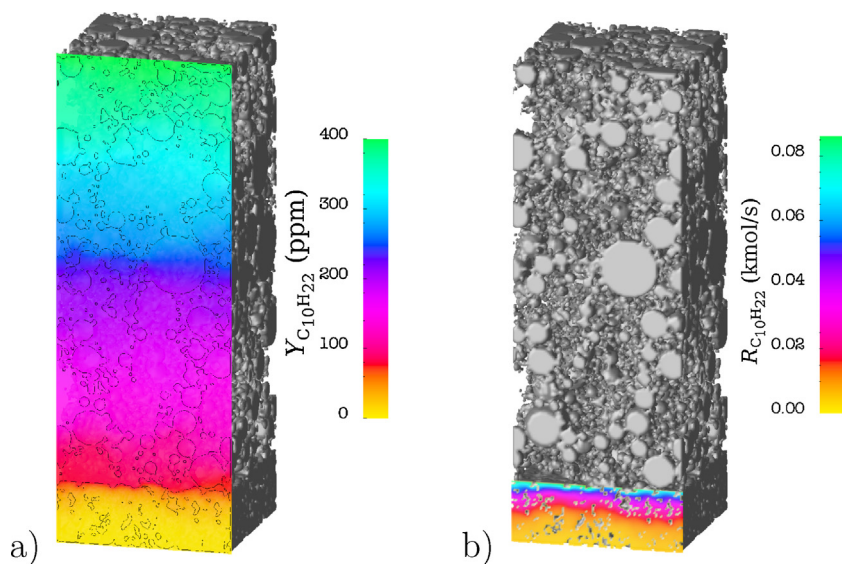


Fig. 10. Example of steady state decane concentration (a) and reaction rate (b) profiles in the section of A18+1125.PS10 coating (Table 2) at 250 °C.

(with effective diffusivity obtained from the random-pore correlation [9]) together with the 1D plug-flow balances of the reactor (further called “standard model”).

3.2.1. Detailed multi-scale model

The detailed model consists of component mass balances in the flowing gas and catalytic layer (20, 21), and enthalpy balances of the flowing gas and solid phase (22, 23) [1,8].

$$\frac{\partial c_i(z, t)}{\partial t} = -v \frac{\partial c_i}{\partial z} + \frac{k_{c,i} a}{\varepsilon^g} c (Y_i^w - Y_i), \quad i = 1, \dots, I \quad (20)$$

$$\frac{\partial c_i^w(z, t)}{\partial t} = \frac{k_{c,i} a}{\varepsilon^w(1 - \varepsilon^g)\varphi^w} c (Y_i - Y_i^w) + \frac{1}{\varepsilon^w} \sum_{j=1}^J v_{i,j} R_j^{\text{avg},t}, \quad i = 1, \dots, I \quad (21)$$

$$\rho c_p \frac{\partial T(z, t)}{\partial t} = -v \frac{\partial T}{\partial z} \rho c_p + \frac{k_h a}{\varepsilon^g} (T^s - T) \quad (22)$$

$$\rho^s c_p^s \frac{\partial T^s(z, t)}{\partial t} = \lambda^s \frac{\partial^2 T^s}{\partial z^2} + \frac{k_h a}{1 - \varepsilon^g} (T - T^s) - \varphi^w \sum_{j=1}^J \Delta H_{r,j} R_j^{\text{avg},t} - \alpha (T^s - T^e) \quad (23)$$

Boundary conditions at the inlet ($z=0$) and at the outlet ($z=L$) of the monolith are:

$$T = T^{\text{in}}, \quad c_i = c_i^{\text{in}}, \quad i = 1 \dots I \quad \text{at } z = 0 \quad (24)$$

$$\frac{\partial T^s}{\partial z} = 0 \quad \text{at } z = 0 \text{ or } z = L \quad (25)$$

The table of average diffusion-reaction rate $R_j^{\text{avg},t}(T, Y_i^w)$ is pre-calculated in 3D micro-scale simulations for each porous structure, and the actual local reaction rates are evaluated by interpolation dependent on the local temperature and concentrations of key reactants [23,31]. Using this multi-scale approach, the behaviour of a reactor containing specified catalyst layers can be efficiently simulated at varying conditions [1]. Proper geometric surface area density (a), reactor void fraction (ε^g) and coating volume fraction (φ^w) are calculated for each sample from the known geometry (cf. Tables 3 and 5). During each simulation, component-dependent variable heat and mass transfer coefficients along the reactor ($k_h(z)$ and $k_{c,i}(z)$) are calculated for actual local gas velocity and temperature according to suitable correlations [25]. Effective heat exchange coefficient α describes heat losses from the coated plates to steel

Table 5

Values of model parameters used in full-scale simulations of lab reactor.

| Parameter | Value |
|---|---|
| Density of geometric surface area (GSA) a | 887 m ² m ⁻³ of reactor |
| Macroscopic void fraction of reactor ε^g | 0.77–0.89 ^b |
| Volume fraction of coating in solid phase φ^w | 0.15–0.50 ^{a,b} |
| Distance between plates (for k_h and k_c correlations [25]) | 0.87–1.00 mm ^b |
| Limit Nu and Sh number (for k_h and k_c correlations [25]) | 7.54 |
| Mean effective heat conductivity of solid phase λ^s | 8 W m ⁻¹ K ⁻¹ ^{a,c} |
| Mean volumetric heat capacity of solid phase $\rho^s \cdot c_p^s$ | 1.8 × 10 ⁶ J m ⁻³ K ⁻¹ of solid phase ^{a,c} |
| Effective heat exchange coefficient α | 200 W m ⁻² K ⁻¹ |

^a Solid phase = metal foil + coating.

^b Exact value depends on thickness of coated layers; parameter varied accordingly for each sample (cf. Table 2).

^c Exact value depends on thickness and porosity of coated layers; constant mean value used in simulations because slow (pseudo-steady state) temperature ramp results are insensitive to variations of this parameter.

reactor body—above the light-off, both measured and simulated differences between the inlet and outlet temperature were ca. 5 K, while the temperature increase in a perfectly adiabatic reactor reaches ca. 50 K. The temperature of surrounding steel reactor body T^e was maintained by heat controller so that it was equal to the inlet gas temperature T^{in} during all experiments.

3.2.2. Standard 1D+1D model

The conventional 1D + 1D approach uses the same equations for plug flow reactor as (20)–(25) except that Eq. (21) is replaced by Eq. (26) where a simplified 1D diffusion in the coated layer is solved explicitly:

$$\frac{\partial c_i^s(z, r, t)}{\partial t} = \frac{D_i^{\text{eff}}}{\varepsilon^s} \frac{\partial^2 c_i^s}{\partial r^2} + \frac{1}{\varepsilon^s} \sum_{j=1}^J v_{i,j} R_j, \quad i = 1, \dots, I \quad (26)$$

Note that here the local reaction rates in the layer are evaluated directly according to rate laws in Eqs. (16)–(18). The corresponding

Table 6

Calculated CO and decane effective diffusion coefficients at $T = 298$ K in different γ -Al₂O₃ layers obtained from the detailed 3D model (det), from the standard random-pore correlation (std), and their relative difference (Δ). Macroporosity (ε_M) and the evaluated tortuosity factor (τ_M) of the 3D reconstructed macropore structures are also given.

| Layer ID | ε_M (%) | τ_M (1) | $D_{CO}^{eff} (\times 10^{-6} \text{ m}^2 \text{ s}^{-1})$ | | | $D_{C_{10}H_{22}}^{eff} (\times 10^{-6} \text{ m}^2 \text{ s}^{-1})$ | | |
|-----------|---------------------|--------------|--|------|--------------|--|------|--------------|
| | | | det | std | Δ (%) | det | std | Δ (%) |
| I125_PS10 | 54 | 1.8 | 6.38 | 5.52 | 13 | 2.02 | 1.78 | 12 |
| I130 | 35 | 2.5 | 3.63 | 2.82 | 22 | 1.18 | 0.93 | 21 |
| I95_p100 | 17 | 4.2 | 1.40 | 0.94 | 33 | 0.53 | 0.33 | 38 |

boundary conditions for the simplified 1D diffusion sub-model are:

$$D_i^{eff} \frac{\partial c_i^s}{\partial r} \Big|_{r=\delta-} = k_{c,i} c_i (Y_i - Y_i^s|_{r=\delta}), i = 1, \dots, I \quad @ r = \delta \quad (27)$$

$$D_i^{eff} \frac{\partial c_i^s}{\partial r} = 0, i = 1, \dots, I \quad @ r = \delta \quad (28)$$

This simplified diffusion model treats the layer as pseudo-homogeneous slab. As discussed above, the overall effective diffusivity is estimated here from the random pore correlation [9], considering both mesopores “ μ ” and macropores “ M ” present in the layer:

$$D_i^{eff} = \varepsilon_M^2 D_{i,M} + \varepsilon_\mu^2 D_{i,\mu} + \frac{4(\varepsilon_M - \varepsilon_M^2)}{\left(\frac{1}{D_{i,M}} + \frac{(1 - \varepsilon_M)^2}{\varepsilon_\mu^2 D_{i,\mu}}\right)} \quad (29)$$

The values of $D_{i,M}$ and $D_{i,\mu}$ are calculated from combined volume and Knudsen diffusivity, similarly to Eqs. (4)–(7), using mean diameter of macropores and mesopores, respectively.

4. Results

In this section we compare the simulation results with the measured data in order to validate the model predictions. The measured decane and CO light-off curves are shown in Fig. 11. The extent of diffusion limitation is revealed by the residual outlet concentration of the reactant above the light-off temperature (ca. 160 °C for decane and ca. 210 °C for CO), where the fully diffusion-controlled regime is established. This part of the curve is therefore used for validation of the transport model in the coated layers.

Slight differences in the light-off temperature can be observed between the individual samples as the coating thickness of the active layer was not perfectly uniform. As explained in the model discussion, this minor variation does not influence the conversions in the fully diffusion-limited regime. Decane curves may exhibit additional concentration variations at the very beginning of the experiment, caused by initial fluctuations of the used decane liquid flow controller and evaporation unit around the set-point until the steady regime is reached, and eventually minor desorption peak of decane. After this initial period the fluctuations diminish and a stable regime is achieved. The inlet concentration levels were verified before and after each experiment using by-pass measurements.

The diffusion limitations decreased from A18+I95_p100 over A18+I130 to the A18+I125_PS10 sample for both decane and CO light-off curves, cf. Fig. 11. Note that the thickness of the layers and γ -Al₂O₃ intraparticle properties are similar for all three samples (Table 2), so that the improvement in diffusivity and conversion can be directly linked to the increasing macroporosity of the top layer.

The macroporous structure of all samples was digitally reconstructed by virtual packing of spherical γ -Al₂O₃ particles with the known size distribution and target macroporosity (obtained from the cross-section SEM images analysis). The spatial discretization step 250 nm was chosen after sensitivity tests with several different step values in reaction-diffusion simulations. Further decrease of

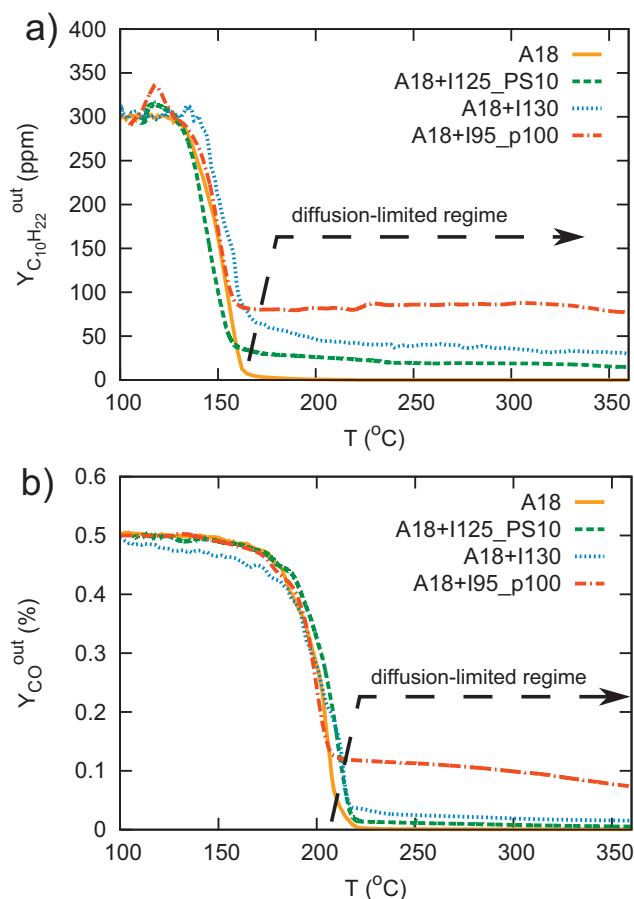


Fig. 11. Light-off curves measured for the samples with varied coating properties (Table 2): (a) decane oxidation, (b) CO oxidation.

the discretization step did not influence the results significantly but strongly increased the computational demands (half step results in eight times higher number of voxels in the 3D matrix).

The dependences of effective reaction rates on the temperature and boundary concentrations of *n*-decane and CO were then calculated by the detailed model and utilized in the 1D plug flow model of the monolithic channel to get corresponding light-off curves. Fig. 12 compares detailed and standard model predictions with experimental data for individual catalytic coatings. It can be seen that in all cases the initial part of light-off curve is similar for both models, because it is determined mainly by the reaction kinetics (the same in both models). However, the diffusion-limited regime at higher temperatures reveals that the diffusion rate predicted by the detailed model based on 3D reconstruction of the porous layer matches the experimental results better than the standard model. It can be concluded that the random-pore correlation employed in the standard model tends to predict higher diffusion limitation (i.e., somewhat lower D^{eff} values). This becomes particularly significant for low-macroporosity layers (Fig. 12a), while the differences decrease for highly macroporous layers (Fig. 12c).

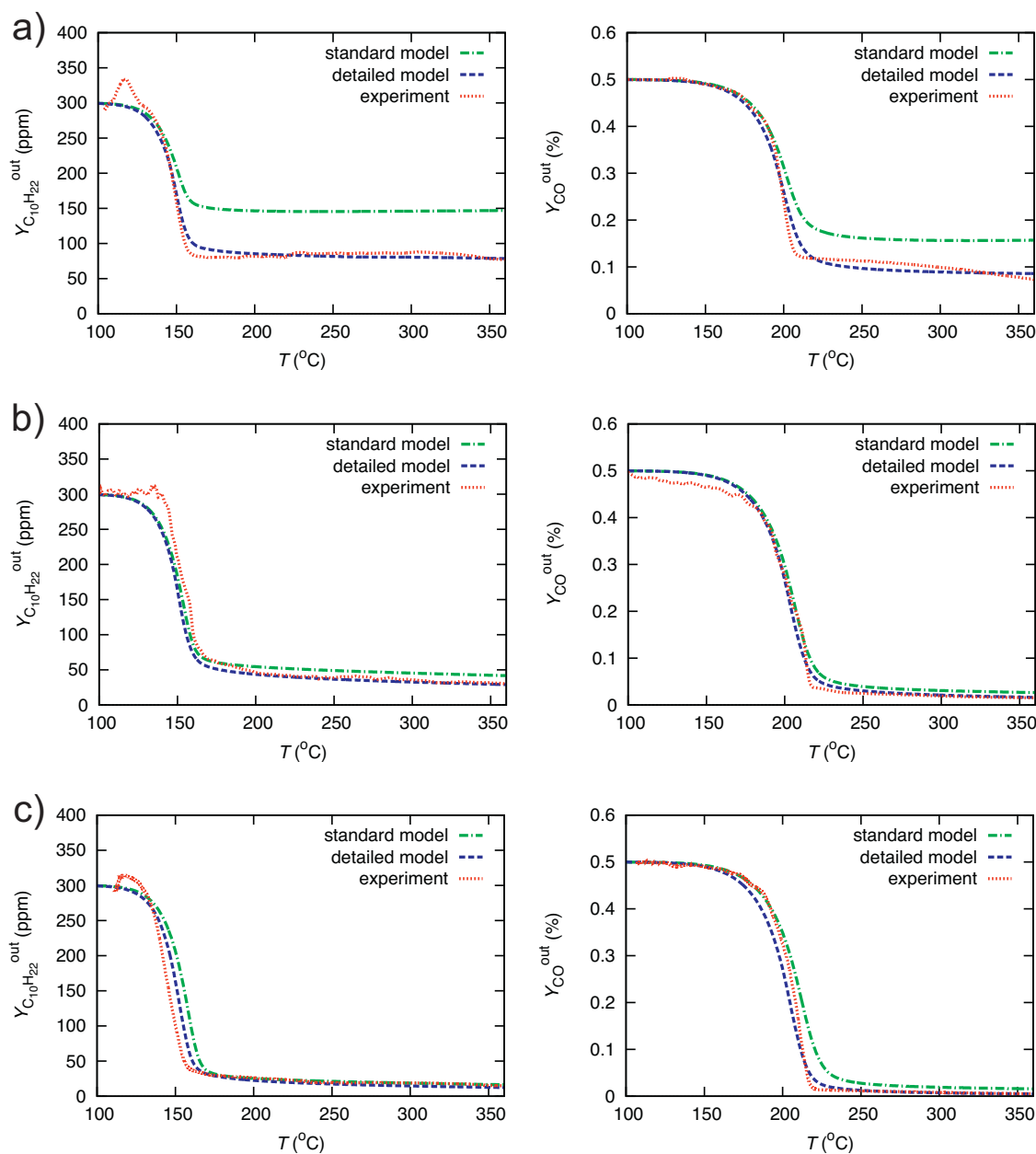


Fig. 12. Comparison of the measured and simulated decane and CO light-off curves for the samples with varied coating properties: (a) A18+I95.p100, (b) A18+I130, and (c) A18+I125.PS10 (Table 2).

The predicted effective diffusivities of CO and decane depending on porous layer structure are summarized in Table 6. It can be seen that macroporosity is a key parameter enabling efficient transport through the layer. The compact sample with macroporosity 17% exhibits approximately five times lower effective diffusivity than the most porous sample obtained with pore templates (macroporosity 54%). The non-linear dependence of the effective diffusivity on macroporosity is reflected in varying tortuosity factor of the macropore space (this tortuosity value is obtained as a result of predictive pore-scale simulations in the 3D reconstructed layer, not a parameter fitted to experimental data). A higher tortuosity corresponds to a worse connectivity of macropores. Both low macroporosity and high tortuosity of the macropores contribute to poor transport properties of the compacted sample.

It can be also seen in Table 6 that the difference between the detailed 3D model and standard random-pore correlation increases with decreasing macroporosity, and reaches approximately 30%

in the case of the pressed sample, which is in line with the trends depicted in Fig. 12. These results collectively suggest that the random-pore correlation underestimates the connectivity of macropores at low macroporosities, giving more weight to slow Knudsen diffusion in mesopores. On the contrary, the detailed 3D model of packed spherical particles is able to correctly capture the remaining channels that still connect the macropores and thus increase the overall diffusivity.

The corresponding temperature dependences of the CO and decane effective diffusion coefficients predicted from simulations in the 3D reconstructed layers by the detailed pore-scale model are shown in Fig. 13a. Such curves can be easily utilized in common monolith channel models where effective diffusivity values are evaluated depending upon local temperature. For this purpose, a simplified correlation can be used in the form of Eq. (30):

$$D_i^{\text{eff}} = aT^b, \quad [T] = \text{K}, \quad [D_i^{\text{eff}}] = \text{m}^2 \text{s}^{-1} \quad (30)$$

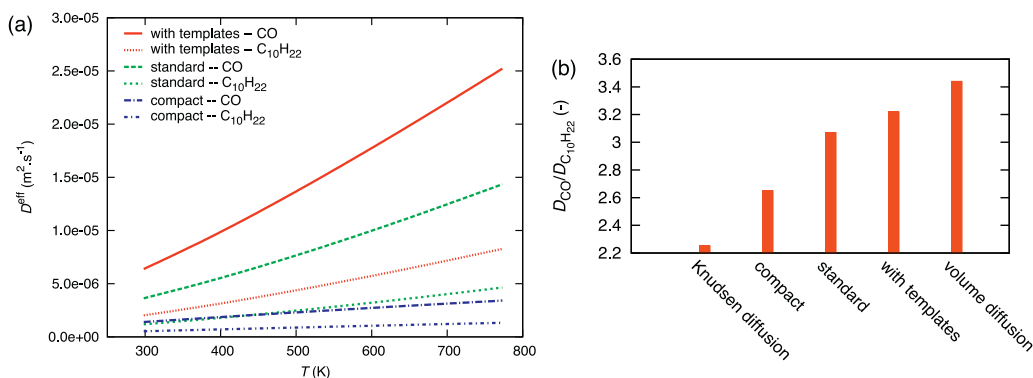


Fig. 13. Temperature dependence of the effective diffusivity in the individual Al_2O_3 layers (varying macroporous structure), predicted by the detailed pore-scale model (a), and the corresponding CO:decane diffusivity ratio at 298 K reflecting the contribution of volume and Knudsen diffusion to the overall transport (b).

Table 7
Coefficients of simplified effective diffusivity dependence on temperature, Eq. (30).

| Layer ID | CO | | $\text{C}_{10}\text{H}_{22}$ | |
|-----------|-----------------------|------|------------------------------|------|
| | $a [\times 10^{-10}]$ | b | $a [\times 10^{-10}]$ | b |
| I125_PS10 | 19.1 | 1.43 | 4.68 | 1.47 |
| I130 | 9.73 | 1.44 | 3.16 | 1.44 |
| I95_p100 | 71.5 | 0.93 | 22.3 | 0.96 |

The parameters a and b for the tested layers are given in Table 7. The value of exponent b is always between 0.5 (pure Knudsen diffusion, cf. Eq. (7)) and 1.75 (pure volume diffusion, cf. Eq. (6)). The actual value thus reveals the relative importance of these two diffusion mechanisms for the transport through the layer. These results can be obtained from predictive simulations for arbitrary coating, depending only on the information about its porous structure (particle and pore size distributions, porosities, cross-section SEM images). The resulting temperature dependence of effective diffusivity in the form of Eq. (30) can be then directly employed in conventional 1D + 1D monolith channel models [8].

Note that the ratio of CO and decane effective diffusivities in Fig. 13b vary for individual samples (3.22, 3.07 and 2.65 for the pore templated, standard and the pressed sample, respectively). In principle, these values must again fall between the two limits: (i) the ratio for pure volume diffusion, and (ii) the ratio for pure Knudsen diffusion. These limit ratios between CO and decane diffusivity are 3.44 and 2.25, respectively, as calculated from Eqs. (6) and (7). The actual ratio is thus another indicator of the actual transport regime in the layer. It can be concluded that volume diffusion in macropores represents a major mechanism for the standard coating (referring to nomenclature of the samples used in this paper) and the layer with templates (macroporosities 35 and 54%, respectively). On the contrary, the overall transport in the compact layer with macroporosity 17% relies on slow diffusion through mesopores to a larger extent. The relatively small mean macropore size of 238 nm in this case (Table 2) leads to an increasing importance of Knudsen diffusion regime also in macropores (Eq. (4), considering that the mean free path of CO molecules at $T = 200^\circ\text{C}$ is ca 170 nm).

Such considerations are quite important for the design of multiple catalytic coatings. For example, it can be concluded that the overall transport through the layers with moderate or high macroporosity is relatively insensitive to the internal meso-/micro-porous structure of the supporting material. Therefore, global effective diffusivities of a similar magnitude could be expected also for the layers with sufficiently high macroporosity formed from other supporting materials (e.g., wide mesopore alumina, CeO_2 , zeolites, etc.). Of course, local transport limitations

to the catalytic sites in meso-/micro-pores may still affect the catalyst performance, as discussed elsewhere [3,17].

5. Conclusions

Novel multi-scale methodology for detailed modeling of diffusion and reaction in porous catalytic layers was introduced and successfully applied to predict effective diffusivities in various Pt/ γ - Al_2O_3 coatings. This model based on 3D reconstruction of porous structure can predict transport characteristics of the layer without the use of any adjustable parameters. The effects of diffusion limitations on CO and decane oxidation conversions were demonstrated by simulations, and the model predictions were validated by experiments. Good agreement of calculated and measured CO and n -decane conversions was obtained over a wide range of coated layers structures, involving also compacted or pore-templated layers. The detailed 3D pore-scale model provided more accurate predictions of effective diffusion coefficients than the conventional random-pore correlation [9] that estimated somewhat higher diffusion limitations for all studied samples. The differences were particularly important for the layers with a lower macroporosity.

The developed model can be applied for design and optimization of coated layer structure with respect to the utilization of key components like platinum group metals, and to maximize the effectiveness factor in particular for the application of catalytic monolith.

Acknowledgements

This work has been financially supported by the Czech Science Foundation (GACR P106/10/1568) and the Specific University Research (MSMT No. 20/2013). The result was developed within the CENTEM project CZ.1.05/2.1.00/03.0088, co-funded by the European Research Development Fund as part of the Czech Ministry of Education, Youth and Sports' OP RDI programme. The authors would also like to thank A. Wagland and D. Thompsett for useful discussions pertaining to the work herein.

References

- [1] V. Novák, P. Kočí, F. Štěpánek, M. Marek, P. Blanco-García, G. Jones, *Catalysis Today* 188 (2012) 62–69.
- [2] S.Y. Joshi, Y. Ren, M.P. Harold, V. Balakotaiah, *Applied Catalysis B: Environmental* 102 (2011) 484–495.
- [3] P.S. Metkar, V. Balakotaiah, M.P. Harold, *Chemical Engineering Science* 66 (2011) 5192–5203.
- [4] P.S. Metkar, M.P. Harold, V. Balakotaiah, *Chemical Engineering Science* 87 (2013) 51–66.
- [5] A. Scheuer, W. Hauptmann, A. Drochner, J. Gieshoff, H. Vogel, M. Votsmeier, *Applied Catalysis B: Environmental* 111–112 (2012) 445–455.

- [6] M. Colombo, I. Nova, E. Tronconi, V. Schmeißer, B. Bandl-Konrad, L.R. Zimmermann, *Applied Catalysis B: Environmental* 142–143 (2013) 337–343.
- [7] Y. Liu, Y. Zheng, M.P. Harold, D. Luss, *Applied Catalysis B: Environmental* 132–133 (2013) 293–303.
- [8] A. Güthenke, D. Chatterjee, M. Weibel, B. Krutzsch, P. Kočí, M. Marek, I. Nova, E. Tronconi, *Advances in Chemical Engineering* 33 (2007) 103–211.
- [9] N. Wakao, J.M. Smith, *Chemical Engineering Science* 17 (1962) 825–834.
- [10] D. Papadias, L. Edsberg, P. Björnbo, *Chemical Engineering Science* 55 (2000) 1447–1459.
- [11] R.E. Hayes, B. Liu, M. Votsmeier, *Chemical Engineering Science* 60 (2005) 2037–2050.
- [12] A. Santos, A. Bahamonde, P. Avila, F. Garca-Ochoa, *Applied Catalysis B: Environmental* 8 (1996) 299–314.
- [13] R.E. Hayes, S.T. Kolaczowski, P.K.C. Li, S. Awdry, *Applied Catalysis B: Environmental* 25 (2000) 93–104.
- [14] F. Zhang, R.E. Hayes, S.T. Kolaczowski, *Chemical Engineering Research and Design* 82 (A4) (2004) 481–489.
- [15] T. Starý, O. Šolcová, P. Schneider, M. Marek, *Chemical Engineering Science* 278 (2006) 5934–5943.
- [16] S.Y. Joshi, Y. Ren, M.P. Harold, V. Balakotaiah, *Industrial & Engineering Chemistry Research* 51 (2012) 7482–7492.
- [17] P. Kočí, V. Novák, F. Štěpánek, M. Marek, M. Kubíček, *Chemical Engineering Science* 65 (2010) 412–419.
- [18] V. Novák, F. Štěpánek, P. Kočí, M. Marek, M. Kubíček, *Chemical Engineering Science* 65 (2010) 2352–2360.
- [19] J. Regalbuto (Ed.), *Catalyst Preparation, Science and Engineering*, CRC Press, 2007.
- [20] T.A. Nijhuis, A.E.W. Beers, T. Vergunst, I. Hoek, F. Kapteijn, J.A. Moulijn, *Catalysis Reviews: Science and Engineering* 43 (2001) 345–380.
- [21] Institute of Chemical Technology, Prague, Monolith research group, <http://www.vscht.cz/monolith>, 2013 (accessed 30.09.13).
- [22] P. Kočí, F. Štěpánek, M. Kubíček, M. Marek, *Chemical Engineering Science* 61 (2006) 3240–3249.
- [23] V. Novák, P. Kočí, F. Štěpánek, M. Marek, *Industrial & Engineering Chemistry Research* 50 (2011) 12904–12914.
- [24] P. Kočí, F. Štěpánek, M. Kubíček, M. Marek, *Chemical Engineering Science* 62 (2007) 5380–5385.
- [25] K. Ramanathan, V. Balakotaiah, D.H. West, *Chemical Engineering Science* 58 (2003) 1381–1405.
- [26] P. Kočí, F. Štěpánek, M. Kubíček, M. Marek, *Molecular Simulation* 33 (2007) 369–377.
- [27] Y. Notay, *ETNA* 37 (2010) 123–146.
- [28] B.E. Poling, J.M. Prausnitz, J.P. O'Connell, *The Properties of Gases and Liquids*, McGraw-Hill, New York, 2001.
- [29] S. Voltz, C. Morgan, D. Liederman, S. Jacob, *Industrial and Engineering Chemistry, Product Research and Development* 12 (1973) 294–301.
- [30] W.H. Press, S.A. Teukolsky, W.T. Vetterling, B.P. Flannery, *Numerical Recipes in FORTRAN: The Art of Scientific Computing*, Cambridge University Press, 1992.
- [31] M. Votsmeier, *Chemical Engineering Science* 64 (2009) 1384–1389.